Development of a training phantom for compression breast elastography–comparison of various elastography systems and numerical simulations

Article *in* Journal of Medical Imaging · December 2015

DOI: 10.1117/1.JMI.2.4.047002

CITATIONS
9

READS
111

4 authors, including:

Kavitha Manickam

5 PUBLICATIONS **84** CITATIONS

SEE PROFILE

Ramasubbareddy Machireddy

Indian Institute of Technology Madras

16 PUBLICATIONS **168** CITATIONS

SEE PROFILE

Suresh Seshadri

Mediscan systems

141 PUBLICATIONS **1,154** CITATIONS

SEE PROFILE

Journal of Medical Imaging

MedicalImaging.SPIEDigitalLibrary.org

Development of a training phantom for compression breast elastography —comparison of various elastography systems and numerical simulations

Kavitha Manickam
Machireddy Ramasubba Reddy
Suresh Seshadri
Bagyam Raghavan

SPIE.

Development of a training phantom for compression breast elastography—comparison of various elastography systems and numerical simulations

Kavitha Manickam,[a,*] Machireddy Ramasubba Reddy,[a] Suresh Seshadri,[b] and Bagyam Raghavan[c]
[a]Biomedical Engineering Group, Department of Applied Mechanics, IIT Madras, Chennai 600 036, India
[b]Mediscan Systems, Chennai 600 004, India
[c]Apollo Speciality Hospitals, Chennai 600 035, India

Abstract. The elastic properties of tissue are related to tissue composition and pathological changes. It has been observed that many pathological processes increase the elastic modulus of soft tissue compared to normal. Ultrasound compression elastography is a method of characterization of elastic properties that has been the focus of many research efforts in the last two decades. In medical radiology, compression elastography is provided as an additional tool with ultrasound B-mode in the existing scanners, and the combined features of elastography and echography act as a promising diagnostic method in breast cancer detection. However, the full capability of the ultrasound elastography technique together with B-mode has not been utilized by novice radiologists due to the nonavailability of suitable, appropriately designed tissue-mimicking phantoms. Since different commercially available ultrasound elastographic scanners follow their own unique protocols, training novice radiologists is becoming cumbersome. The main focus of this work is to develop a tissue-like agar-based phantom, which mimics breast tissue with common abnormal lesions like fibroadenoma and invasive ductal carcinoma in a clinically perceived way and compares the sonographic and elastographic appearances using different commercially available systems. In addition, the developed phantoms are simulated using the finite-element method, and ideal strain images are generated. Strain images from experiment and simulation are compared based on image contrast parameters, namely contrast transfer efficiency (CTE) and observed strain, and they are in good agreement. The strain image contrast of malignant inclusions is significantly improved compared to benign inclusions, and the trend of CTE is similar for all elastographic scanners under investigation. [DOI: 10.1117/1.JMI.2.4.047002]

Keywords: tissue mimicking phantoms; finite-element simulations; breast imaging-reporting and data system; Itoh score; stiffness imaging; ultrasound elastography.

Paper 15117RR received Jun. 11, 2015; accepted for publication Nov. 16, 2015; published online Dec. 17, 2015.

1 Introduction

Breast cancer is the second most common cancer among women in India according to the cancer statistics report by the World Health Organization for the year 2012.[1] Survival of breast cancer depends on early detection and treatment. Mammography, self examination, and clinical breast examination are the primary methods used in screening. Although current modalities of breast imaging, including magnetic resonance imaging (MRI), sonography, and digital mammography, have high sensitivities for detecting breast lesions, they do not have high specificities.[2] In order to increase the specificity, mammography combined with ultrasonography or MRI is suggested by radiologists. Researchers have shown that the disease process in the human body alters the elastic properties of soft tissues.[3,4] The elastic properties are imaged by giving a mechanical compression to tissues of interest and analyzing the response of the same, which is known as stiffness imaging or elastography.[5] The tissue response could be measured using either ultrasound,[5] MRI,[6] or optical methods.[7] Here, we focus on ultrasound elastography imaging techniques in which tissue displacement is estimated by finding out the time delay between reflected echoes.[5]

Based on the compression, there are two different approaches in ultrasound elastography, namely compression or strain elastography[5] and shear wave elastography (SWE).[8] Compression elastography (known as freehand elastography) is a qualitative method of imaging the elastic properties in which global compression is given by pressing the probe.[5] The displacements of tissue are captured, and a relative stiffness map compared with the stiffness of surrounding tissue is created and displayed as an elastogram. Instead of the manual compression by probe, respiratory movement, heartbeat, or blood flow can be used as compression sources in the image protocol.[9] Compression elastography allows only for qualitative and semiquantitative assessments of a lesion because the force exerted by manual compression using the probe is unknown while reconstructing the elastogram, thus allowing only the calculation of the strain ratio (observed strain contrast) and not the absolute elasticity distribution. In contrary, SWE, which includes acoustic radiation force impulse (ARFI)[8] imaging and supersonic shear-wave imaging,[10] uses acoustic radiation force to compress tissue remotely, but it differs in the postprocessing and acquisition of echoes.

*Address all correspondence to: Kavitha Manickam, E-mail: kavitharunkumar@gmail.com

2329-4302/2015/$25.00 © 2015 SPIE

In the literature, the promising features of compression elastography, namely strain and the area ratio between the ultrasound B-mode and elastogram, have been discussed toward improving the specificity of breast diagnosis.[5,11] The classification accuracy of the diagnostic system was significantly improved by including strain information as an additional input with ultrasound B-mode features.[12] In order to use elastography in routine clinical practice, the sonographer needs to have a thorough understanding of the techniques, imaging methods, and appearance of elastographic patterns for different clinical cases and their interpretation. Hence, there is a need to develop a standard breast phantom with common abnormalities for elastography applications in order to improve diagnostic confidence when using elastography in clinical practice. Siemens S2000 (Siemens Healthcare, Erlangen, Germany), Philips iU22 (Philips Healthcare, Andover, Massachusetts), Hitachi RTE (Hitachi Aloka Medical America, Inc., Wallingoford, Connecticut), and GE Logiq E9 (GE Healthcare, Madison) are the four ultrasound elastography scanners commonly used in hospitals. Each machine follows a different protocol to generate the elastogram. A common phantom is needed for radiologists to understand the protocols and appearances of abnormalities in each machine.

The popular tissue-mimicking materials used in elastography phantoms are oil-in-gelatin, oil-in-gelatin agar dispersion,[13] polyacrylamide gels,[14] and polyvinyl alcohol cryogel (PVA-C).[15] In oil-in-gelatin agar phantoms, Madsen et al. achieved elastic modulus values from 5 to 135 kPa. Polyacrylamide gels are highly toxic and fragile; they could not be prepared in clinical environments due to fumes, and they require special precautions.[16,17] In PVA-C phantoms, the elastic modulus for a given concentration of PVA is controlled by varying the freezing or thawing rate of polymerization. Therefore, construction and processing of the samples is a complex procedure.[18]

Computerized Imaging Reference Systems (CIRS) (CIRS, Virginia)[19] and Blue Phantom (CAE Healthcare, Florida)[20] produce commercial elastography phantoms designed for breast applications, which have embedded cylindrical (1.58- to 6.49-mm diameter) and spherical (10- and 20-mm diameter) targets (inclusions) of varying stiffness (8 to 80 kPa) and size. However, the Young's modulus values of the targets are within a limited range for determining the elasticity contrast study, which is far less than the full dynamic range encountered during clinical scanning of breast tissue (25 to 550 kPa).[3] Most of the studies reported in literature to explain commercial phantoms discuss the axial and lateral resolutions, and do not discuss clinical performance. The commercial phantoms are simple in design, and hence the artifacts encountered in clinical situations would not be present in these phantoms. Browne et al.[21] show that some of the clinically reported improvements in image quality using tissue harmonic imaging were not observed using commercial phantoms due to their simplistic design. Further, commercial phantoms do not adequately reflect the shape of the B-mode appearance of lesions observed clinically. In addition, both the target size and strain contrast are varied, which may not be sufficient to provide adequate training to the clinician or to adequately challenge the elastography technique under evaluation. In addition, these phantoms are expensive and are not tailor-made for the need of the radiologists for use as a training phantom.[22]

Previously, Madsen et al.[23] constructed anthropomorphic breast phantoms with simulated lesions, which consist of oil-in-gelatine agar dispersions. In the phantom, both fibroadenomas and cancer were simulated, where the former was circular and latter was irregularly shaped. In their work, they reported that the elastic modulus of fibroadenomas is 97.8 kPa with a contrast of 2.45, and the elastic modulus of cancers is 64.6 kPa with a contrast of 1.62.

In our work, the first objective is to make lesions which mimic the exact B-mode performance perceived by radiologists, where fibroadenomas are mostly represented by a lobulated appearance and malignant cancers are identified by spiculations. Besides, a wide range of stiffness is investigated—from 12.5 to 450 kPa (detailed in Sec. 2.2)—which covers the entire range of breast abnormalities.[3] Additionally, simple cysts of various diameters were also mimicked to understand their elastographic appearance. The second aim of this work is to introduce the elastographic appearance of solid tumors and cystic lesions using various commercially available elastography systems to resident radiologists. To achieve thse objectives, we have developed a composite phantom, which is used as a training tool; the specifications were designed to mimic breast sonographic examination. The prepared phantoms were imaged using four ultrasound systems, Siemens S2000, Philips iU22, Hitachi RTE, and GE Logiq E9. The pathological information about the abnormalities was received from expert radiologists and literature. The dimensions of the phantom, echogenicity, and elastic properties of background and inclusions were designed as per the work previously reported from our group.[24,25] A three-dimensional (3-D) finite-element model (FEM) of the phantom was created using COMSOL (COMSOL AB, Stockholm, Sweden), and strain images were simulated by assuming a linear elastic material model. Since the applied compression is usually <5%, the tissue is assumed as a linear elastic material.[4,5,24] The results from the image analysis of developed phantoms indicate that malignant lesions (high-contrast lesions) have an improved conspicuity relative to low contrast, benign lesions using ultrasound compression elastography.

2 Development of Breast Phantom

Agar-based composite phantoms are developed to mimic breast tissue with controllable elastic and acoustic properties. Agar is used as a base material, which gives the structural properties such as elastic modulus to the phantoms. When the breast is imaged in the supine position, the mammary zone typically lies at a depth of 1 to 4 cm from the face of the transducer. Most of the abnormalities arise in the mammary zone of the breast, so high resolution is imperative in the region; therefore, high frequencies are utilized for breast imaging. Since agar exhibits near linear response of attenuation to frequency ($f^{1.1}$), it could be used at higher frequencies as a good candidate for tissue mimicking material.[24,26] Ultrasound images consist of speckle in the background, which is a noisy texture due to the microscatterers in the tissue. Speckle is due to constructive and destructive interference of the scattered sound waves from the tissue microstructure. The actual image texture of the speckle does not necessarily have any diagnostic value. However, it can be useful for tracking tissue motion or strain due to compression. In order to get speckles in images which represent those generated from human soft tissue, graphite is used as a scattering agent,[27] and it is added with the phantom material during preparation.

2.1 *Breast Sonographic Anatomy*

In sonography, the breast can be divided into different layers from superficial to deep: the skin and (1) subcutaneous fat; (2) mammary layer (parenchyma) of glands, ducts, and connective tissues; and (3) retromammary fatty layer overlying the (4) pectoralis muscle and (5) chest wall. The sonographic anatomy of breast tissue with lesion is given in Fig. 1.

2.2 *Phantom Design*

In our design, the first fatty layer and second parenchyma layer (mammary layer) were considered. Since most of the significant pathology arises in the mammary layer and also because the other layers, such as retromammary and pectoralis, are deep seated, the deeper tissues are excluded in the design. The layout is given in Fig. 2. Four types of inclusions were developed and included in the uniform background of phantom, which mimics the breast parenchyma layer. Not only the elastic and acoustic properties but also the shape and size of the prepared inclusions have been selected in such a way that they mimic both the sonographic and elastographic appearance of breast tissue in the B-mode and elastogram, respectively. The details are as follows.

- Category I inclusions are designed intentionally to mimic lesions in glandular tissue borderline between normal and suspicious (by having a normal morphology but suspicious sonographic appearance). They are characterized by isoelasticity matching that of surrounding tissue but having a hypoechoic pattern. The modulus ratio of such category is 0 dB. This cylindrical inclusion has a regular boundary, and its diameter is 1 cm. It represents Breast Imaging-Reporting and Data System (BIRADS) 1 or Itoh elasticity score 1.[28]
- Category II inclusions are definitely malignant, which are very stiff and present a hyperechoic sonography pattern, which belongs to BIRADS 5 and Itoh elasticity score 5. Approximately 85% of all breast cancers are invasive ductal carcinoma. Malignant tumors usually present with B-mode features, such as margin irregularity, acoustic shadowing, spicules, hyperechogenecity, desmoplastic reaction around the lesion, calcifications, microlobulation, and significant vascularization.[29] Out of the above-mentioned sonographic features, we considered hyperecho and spiculated boundary, and the modulus ratio of such inclusions is 25 dB. The diameter of the lesions varies from 1 to 2 cm.
- Category III inclusions mimic benign fibroadenoma features, which are slightly stiff and isoechoic. A fibroadenoma is a benign mass of fibrous and glandular tissue. Also, the modulus ratio is 6 dB. Approximately 50% of all benign solid lesions are fibroadenomas. They usually appear with regular shape and well-defined boundaries. These nodules are usually round or ellipsoid in shape with a wider-than-taller orientation, indicating an appearance that is parallel to the chest wall. In this work,

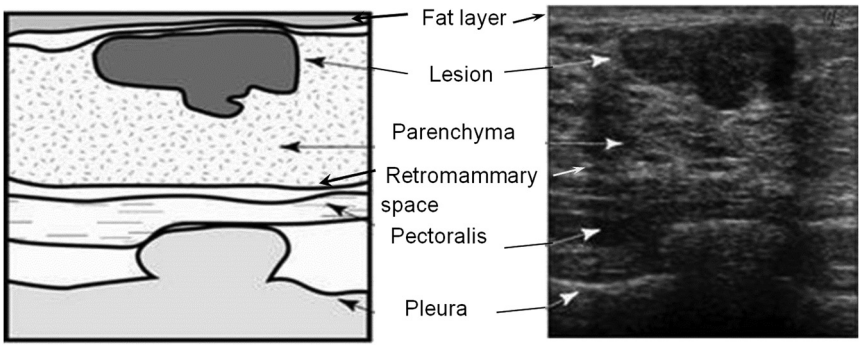

Fig. 1 Sonographic anatomy of breast tissue. (1) Fat layer, (2) parenchyma, (3) retromammary space, (4) pectoralis, and (5) pleura.

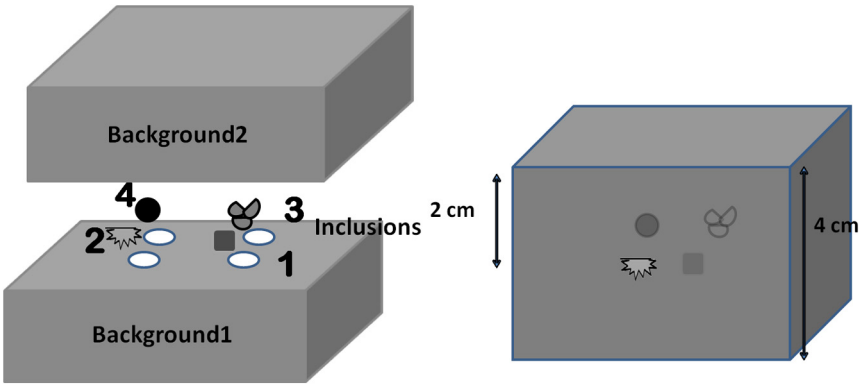

Fig. 2 Layout of the proposed training phantom with inclusions namely, (1) normal but suspicious appearance in B-mode, (2) malignant, (3) fibroadenoma, and (4) simple cyst.

Fig. 3 Cystic inclusions of 2-cm diameter.

category III inclusions are designed to have a regular boundary with three lobules. This category belongs to BIRADS 2 and Itoh elasticity score 2.

- Category IV of inclusions is water filled simple cysts. The cystic deformable membrane is made by a thin latex sheet. Cysts of various diameters from 0.5 to 2 cm were made and imaged. A photograph of one of the cystic inclusions with 2-cm diameter is shown in Fig. 3.

The components used to prepare the phantom are agar, *N*-propanol, and deionized water. In order to have the speed of sound in the phantom match with that in human tissue (1540 m/s), agar is mixed with *N*-propanol (13 ml for 100 ml of water). As explained in the beginning of Sec. 2, the increase in agar concentration results in an increase in the stiffness of the phantoms. Samples were made by varying the concentration of agar from 0.5 to 12 g in 100 ml (0.4% to 6.6% by weight) of water. For the preparation of phantoms, the ingredients in the required proportions were mixed and stirred at room temperature until they were completely dissolved in deionized water. The mixture was heated in a microwave oven up to 90°C since the boiling point of agar is 85°C. When the stock solution reached 90°C, it was removed from the oven and allowed to cool at room temperature while being stirred at 1000 rpm using a magnetic stirrer. When the temperature of the solution reached 50°C, it was poured into a Perspex mould. The solution in the mould was allowed to settle at room temperature for at least 12 h. Then the sample was removed from the mould, placed in the distilled water, and stored in a refrigerator at 4°C to avoid dehydration. The sample was taken from the refrigerator and allowed to reach room temperature before any measurements were performed on it.

Prior to the preparation of composite phantoms, homogeneous phantoms were developed with various concentrations of agar from 0.4% to 6.6% by weight in deionized water to mimic different categories of lesions and tissue background. Three types of phantom samples were prepared for the measurement of acoustic, elastic, and viscoelastic parameters. For acoustic characterization, the prepared phantoms were disc shaped, having 50-mm diameter and 20-mm thickness. The phantom samples for elastic parameter characterization were cylindrical in shape, and the dimensions were chosen such that they satisfy the constraint d4762–11a stated by the American Society for Testing and Materials guidelines for polymeric materials testing. For rheological measurements, the prepared phantom samples were disc shaped and had diameter 25 mm and thickness 1 to 2 mm as per the requirement of the rheometer used. Acoustic properties of the prepared agar phantoms such as acoustic velocity, acoustic impedance, and attenuation coefficient were characterized by a pulse echo ultrasound test at 2.25 to 10 MHz frequencies, and the results are found to be in the range of (1564 ± 88 to 1671 ± 124 m s^{-1}), (0.6915 ± 0.123 to 0.8268 ± 0.755 db cm^{-1} MHz^{-1}), and ($1.61 \times 10^6 \pm 0.127$ to $1.76 \times 10^6 \pm 0.045$ kg m^{-2} s^{-1}).[24] In addition to acoustic parameters, biomechanical properties, such as linear elastic, hyperelastic, and viscoelastic parameters were characterized for the prepared phantom samples. Linear elastic moduli were measured by conducting a quasistatic uniaxial compression test under a strain rate of 0.5 mm/min up to 15% strain, and they are in the range of 12.5 to 450 kPa. The detailed explanation of the development procedure and characterization of elastic and acoustic properties are explained elsewhere.[24,25] Based on the elastic modulus values, the concentration of agar was chosen for the background and also for the different categories of abnormalities explained in the previous paragraphs.

The phantom was made in three steps. In each step, the procedure explained in the previous paragraph[25] was adopted. However, during solidification of samples, graphite powder of the required concentration (Table 1) was added at 35°C and vigorously stirred using a magnetic stirrer at 1000 rpm in order to avoid the settlement of graphite at the bottom. The background of the phantom sample was made of 1-g agar solution (w/v, in 100 ml of deionized water) whose Young's modulus is ~25 kPa. Initially, the bottom layer of the sample was prepared. During the time of gelation of the bottom layer, holes of the desired shapes were introduced by inserting different shaped moulds. Thereafter, these holes were filled with the necessary concentration of agar solution in order to make the inclusion portion for each category. Finally, the top layer was filled with 0.5-g agar solution (w/v, in 100 ml of deionized water). The phantom preparation steps are explained in Fig. 4. The stiffness and echogenic properties of different layers and inclusions are presented in Table 1.

Due to the addition of graphite particles, the phantoms are black in color. The photograph of one such phantom is shown in Fig. 4(e). The addition of graphite alters the stiffness properties, but is almost negligible. Anderson et al. investigated the effect of graphite concentration on shear wave speed in gelatin phantoms and showed that the shear wave speed does not show any significant changes in stiffness within the first week of

Table 1 Stiffness and echogenecity of different layers and inclusions of breast phantom.

Type	Agar concentration (g)	Average Young's modulus (kPa)	Echogenecity	Graphite concentration (g)
Bottom layer	1	25	—	1
Category 1	1	25	Iso	0
Category 2	8	448	Hyper	0.5
Category 3	2	52	Iso	0.5
Top layer	0.5	12.5	—	0.2

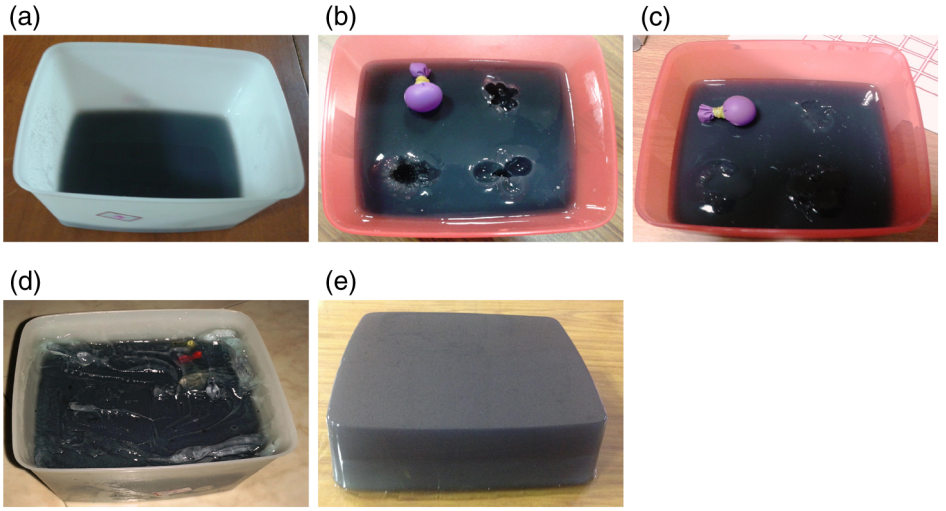

Fig. 4 Stages involved in the preparation of breast phantom: (a) phantom with first bottom layer, (b) desired shaped holes are introduced, (c) holes filled with the specific concentration of agar solution and cyst mimic balloons, (d) whole phantom after completing the top layer, and (e) photograph of the prepared phantom.

fabrication.[30] The results were also verified for the prepared agar samples, and the change in Young's modulus due to graphite particles is within the standard deviation of Young's modulus (Table 2) results reported by Manickam et al.[25]

3 Imaging by Various Elastography Systems—Compression Elastography

The phantoms are imaged using four different elastographic systems—Siemens Acuson S2000, Philips iU22, Hitachi Nobulus, and GE Logiq E9—as these machines are being frequently used clinically. The details of image acquisition and selection of transducer parameters are as follows.

3.1 *Siemens S2000*

Siemens S2000 has both techniques of imaging, compression elastography and ARFI imaging.[8] In this machine, elastograms are created using minimal probe compression. The appropriate compression is determined by a quality factor, which is displayed with an elastogram. We chose elastograms which have a quality factor >60. Both 9L4, 5 to 9 MHz, and 18L6 HD, 18 to 5.5 MHz, probes were used for imaging. In addition to freehand elastograms, we also performed ARFI imaging to give region-specific compression, and the shear wave velocities of different concentration of phantoms were recorded. We have demonstrated the bull's eye pattern, which is the signature of a simple cyst.[2] In the Siemens machine, we acquired both color and gray-scale strain images. In this machine, in color elastograms, red represents hard and blue represents soft, whereas in gray-scale images, black represents stiff and white depicts soft.

Table 2 Measured Young's moduli values of the prepared phantoms.

Agar concentration (g)	Young's modulus (kPa)
0.5 g	12.5 ± 2
1 g	25 ± 3
1.5 g	36 ± 9
2 g	52 ± 31
4 g	182 ± 14
6 g	347 ± 75
8 g	448 ± 10

3.2 *Philips iU22*

In the Philips machine, strain elastography images were acquired by applying very minimal compression. The compression was monitored by a color code with compression bar. Green color represents sufficient compression needed to generate an elastogram. We used a L-12-5 MHz probe and generated elastograms using gray-scale mode, where black represents hard and white represents soft. It provides a semiquantification of the elasticity parameter, which is the strain ratio (observed strain contrast). The strain ratio is defined as the average intensity of the region of interest (ROI) in background to the average intensity of the ROI selected in the lesion area. Cystic lesions were depicted by a bull's eye pattern.

3.3 *Hitachi Nobulus*

Hitachi real-time elastography imaging is a static method (strain elastogram), which uses the combined autocorrelation algorithm proposed by Shiina et al.[31] for the generation of elastograms. Echo signals are captured in real time while the probe compresses or relaxes (rhythmic compression) the body through freehand operation. Strain images are superimposed on B-mode images with a translucent color scale. Additionally, the Hitachi machine provides a compression graph, which clearly depicts the movement of the lesion for the applied compression. An L 55 13-3 MHz probe was used for imaging. The background of the phantom is represented as a mosaic pattern of green and red. Strain images are color images, where blue represents hard and red indicates the soft. Semiquantification of elasticity is achieved by using the parameters of fat-to-lesion ratio (FLR)

and strain ratio. FLR is defined as the average intensity of ROI in the fat portion (first 1 cm of the image) to the ROI chosen in the lesion portion, whereas strain ratio is the ratio of the average intensity of ROI in the lesion portion to the ROI in background paranchyma at the same depth. A simple cyst is represented by a tricolor pattern, blue–green–red (BGR), in elastogram images.

3.4 *GE Logiq E9*

The GE Logiq E9 also uses a simple probe compression technique or patient respiration for the generation of elastograms. For the prepared tissue phantoms, manual probe compression was given, and the relative elasticity is displayed as a real time color map superimposed on the B-mode image. A quality graph provides visual feedback to the user to help monitor the compression technique. Like the other elastography machines, a semiquantitative parameter can be used, which is a relative measure of elasticity in a selected ROI, over a single or multiple frames. We have used an 11 L-D, high frequency linear transducer for image acquisition.

4 Simulation of Breast Phantom

In the compression elastographic image formation process, there are three main steps. In the first step, a stress field is externally applied to the tissue, resulting in a strain field that will be measured using ultrasound in the second step. In the third step, the tissue elastic modulus distribution in the ROI is iteratively reconstructed using the measured displacement or strain estimates. The last step consists of solving an inverse problem, which is an option rather than a necessity in elastography. Actually, the axial strain image, which is computed in the second step, may be interpreted as a relative measure of the tissue elastic modulus. Hence, the first two steps are essential in strain elastography, which forms a forward problem in which strain is calculated by applying stress using either displacement control (for the given displacement, the required load is applied) or load control (for the applied load, appropriate displacement of tissue is obtained). This problem could be modeled using finite-element techniques. Here, the operating strain range is infinitesimal, and in this range, the tissue is modeled as a linear elastic material.

4.1 *Linear Material Modeling of Human Soft Tissue*

Human soft tissue exhibits anisotropic, nonlinear, and viscoelastic behavior,[4] where the stress and strain are time dependent. Therefore, an exact modeling of the mechanical behavior of the tissue under loading is difficult and cumbersome. When external forces are applied on the continuum of the tissue, each point in the continuum experiences stress, and it can be represented as a stress tensor in 3-D. The stress tensor σ_{ij}, which describes the state of stress at any point P of the continuum, is defined as

$$\sigma_{ij} = \begin{bmatrix} \sigma_{11} & \sigma_{12} & \sigma_{13} \\ \sigma_{21} & \sigma_{22} & \sigma_{23} \\ \sigma_{31} & \sigma_{32} & \sigma_{33} \end{bmatrix} \quad \text{with } i, j = 1, 2, 3, \tag{1}$$

where stress σ_{ij} is defined as acting on the i plane and being oriented in the j direction. Components of the stress tensor with repeating indices, such as σ_{ii}, which are acting and orienting in the same plane i are denoted as normal stress while stress components with different indices are called shear stress. Consequently, the stress tensor gives six shear and three normal stress components acting on the cube. Normal stress with positive values directed outward from faces is called tensile stress, whereas negative values correspond to compressive stress.

When an elastic body is subjected to stress, changes in size and shape occur, and these deformations are called strain. Strain is defined as the relative change of a dimension of the body. In 3-D, the strain at point P is determined by the strain tensor ϵ_{ij}, assuming the deformation to be sufficiently small, which is given by

$$\epsilon_{ij} = \begin{bmatrix} \epsilon_{11} & \epsilon_{12} & \epsilon_{13} \\ \epsilon_{21} & \epsilon_{22} & \epsilon_{23} \\ \epsilon_{31} & \epsilon_{32} & \epsilon_{33} \end{bmatrix} \quad \text{with } i, j = 1, 2, 3. \tag{2}$$

The elements of the strain tensor with repeating indices are denoted as normal strains and all others as shear strains. Both the stress and strain tensors have only six independent components due to the symmetric property, such as $\epsilon_{ij} = \epsilon_{ji}$ and $\sigma_{ij} = \sigma_{ji}$.

In a linear elastic medium where the strain is sufficiently small, stress and strain are linearly related to each other by Hooke's law. In general, Hooke's law states that

$$\sigma_{ij} = C_{ijkl}\epsilon_{kl} \quad \text{with } i, j, k, l = 1, 2, 3, \tag{3}$$

where C_{ijkl} is a fourth order tensor known as the stiffness matrix, which describes the elastic constants of the material.[32,33] A full description of the material without any further simplifying assumptions requires a total of 81 elastic constants. The reduction in these elastic constants can be sought with the following symmetries.

Since the stress and strain tensors are symmetrical ($\sigma_{ij} = \sigma_{ji}$ and $\epsilon_{ij} = \epsilon_{ji}$), only 36 ($6 \times 6$) material constants are independent for linear elastic materials. Thus, with the stress and strain symmetry, the independent entries of the stiffness matrix reduce to 36 from 81. If the stiffness matrix is symmetric, it has only 21 independent constants. Further, if the material is assumed to be homogeneous and isotropic, where the material properties are independent of the coordinate system specified, the number of elastic constants reduces to just two parameters, which are termed as Lame parameters λ^c and μ. The resultant Hooke's law now can be stated as

$$\sigma_{ij} = \lambda^c \delta_{ij}\epsilon_{kk} + 2\mu\epsilon_{ij}, \tag{4}$$

where δ_{ij} is Kronecker's delta function. In a uniaxial state of stress (e.g., $\sigma_{11} \neq 0$, σ_{22}, and $\sigma_{33} = 0$), Young's modulus E relates the stress to the resulting strain in the same direction:

$$\sigma_{ij} = E\epsilon_{ij}. \tag{5}$$

For a uniaxial stress state, the Poisson's ratio ν is defined as the ratio of lateral strain (j direction) to axial strain (i direction), which is stated as

$$\nu = -\frac{\epsilon_{jj}}{\epsilon_{ii}}. \tag{6}$$

In contrast to the other elastic parameters, which have the physical unit of pressure, the Poisson's ratio is dimensionless.

By considering the above material assumptions, we approximate the human soft tissue to be purely elastic, showing linear

isotropic behavior and, therefore, characterized by its Young's modulus.[4,5] Now, the model became a discrete deformation problem whose solution is approximated to the solution obtained at the nodes of the mesh, which approximates the tissue continuous domain using FEM. Hence, in this work, we used FEM for modeling the tissue as a linear elastic isotropic homogeneous solid problem. The approximated model is solved by FEM.

4.2 *Modeling*

Extensive study was carried out by the Ophir elastography group in modeling the tissue as a linear elastic material and understanding the mechanical and signal processing factors, which affect elastogram generation and display.[5,34–38] Varghese et al.[37] reported that under ideal conditions of target (inclusion) uniformity, target incompressibility, semi-infinite target dimensions, and infinite compressor, the local stresses in the target are all uniform. Therefore, the local strains are simply inversely proportional to the local elastic moduli. However, in a more realistic situation, this assumption is no longer valid. Since an elastogram depicts the local strain contrast and not the local modulus, a transformation between the two must be made.

In this research, our major objective is to compare the strain patterns generated from strain elastography in representing different classes of abnormalities. This intended study is used to determine the strain patterns incurred by tissue due to compression, from purely mechanical considerations. Thus, we restricted our model up to strain image generation from FEM and did not consider the ultrasound signal processing factors. Two-dimensional nodal strains resulting from the FEM were utilized to form ideal strain images (elastograms). Since there is no estimation procedure involved in getting the nodal strain distribution image, there is no noise present in it. Hence, the simulated image from FEM is called an ideal strain image in this study.

A 3-D model (40 mm × 60 mm × 40 mm) was created in COMSOL, and the schematic, plane of ideal strain image generation, and mesh details are shown in Fig. 5. The geometry of the phantom is the same as that of the ROI of the experimental phantom during sonographic examination. Mechanical properties for the elastic material are based on Young's modulus up to 5% of strain, in which the stress/strain curve is linear.

A solid inclusion of 10-mm diameter at 20-mm depth was made, which mimics the abnormality, and the Young's modulus of the inclusion was assigned from experiments. Compression was given by displacement control in which the phantom movement was simulated for 5% of axial displacement in compression, which mimics probe compression by the radiologist. The Poisson's ratio for both the inclusion and background was fixed at 0.495 to model the incompressible nature of soft tissue.[4] Boundary conditions were given such that they match the real time strain phantom elastography imaging. Hence, the lower surface of the phantom was restricted from downward movement and the sides of the rectangles were unconstrained. Now, the model becomes a forward problem, which is represented by Eq. (4) and solved using the linear solver available in FEM. Thereafter, simulated strain images (isocontour plots) in the y direction (referring to the axial direction of the ultrasound probe) were captured and can be referred to as ideal strain images and used for further analysis.

Thereafter, a contrast-transfer study is performed, which is defined as the ratio (in dB) of the observed elastographic strain contrast from the ideal elastograms to the underlying true modulus contrast. Strain contrast (known as observed strain contrast) could be calculated from this ideal image as the ratio of average strain in the inclusion to the average strain of the background at the same compression levels. It represents a measure of the efficiency with which elastograms depict the underlying modulus distribution in tissue.

5 Image Analysis

Both experimental and simulated strain images were analyzed to investigate the appearance of different categories of lesions. In the Siemens and Philips systems, gray-scale images were obtained. These images were processed to get the observed strain contrast by selecting an ROI in the inclusion portion and also in the background at the same compression level. In the GE and Hitachi machines, we could get color images as outputs. The color image pattern was initially obtained by subtracting the B-mode images from elastograms. The flowchart of the algorithm is shown in Fig. 6, and it is implemented using MATLAB. The results are shown in Fig. 7. Thereafter, the observed strain contrast was calculated for all types of inclusions.

5.1 *Image-Based Parameters for Phantom Validation*

The parameters commonly used to evaluate elastograms are the observed strain contrast C_o and contrast transfer efficiency (CTE).[35] C_o is defined as the ratio of the strain experienced by the background to that of the inclusion; axial strain is the parameter commonly measured in ultrasound elastography:

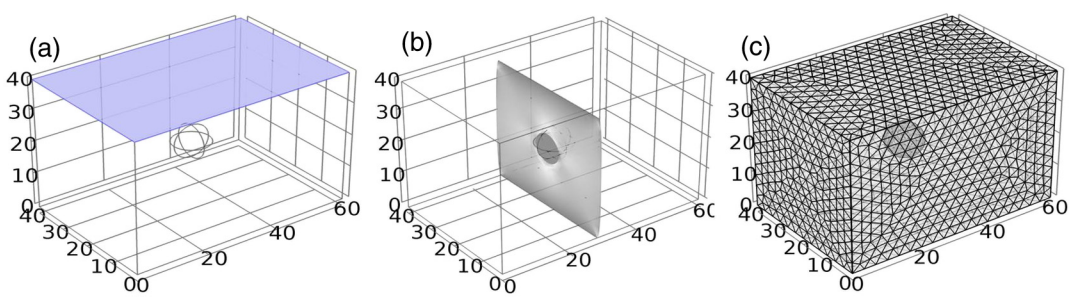

Fig. 5 (a) 3-D finite-element model of the prepared phantom, (b) ultrasound imaging plane, and (c) finite element meshing of the phantom for strain calculation.

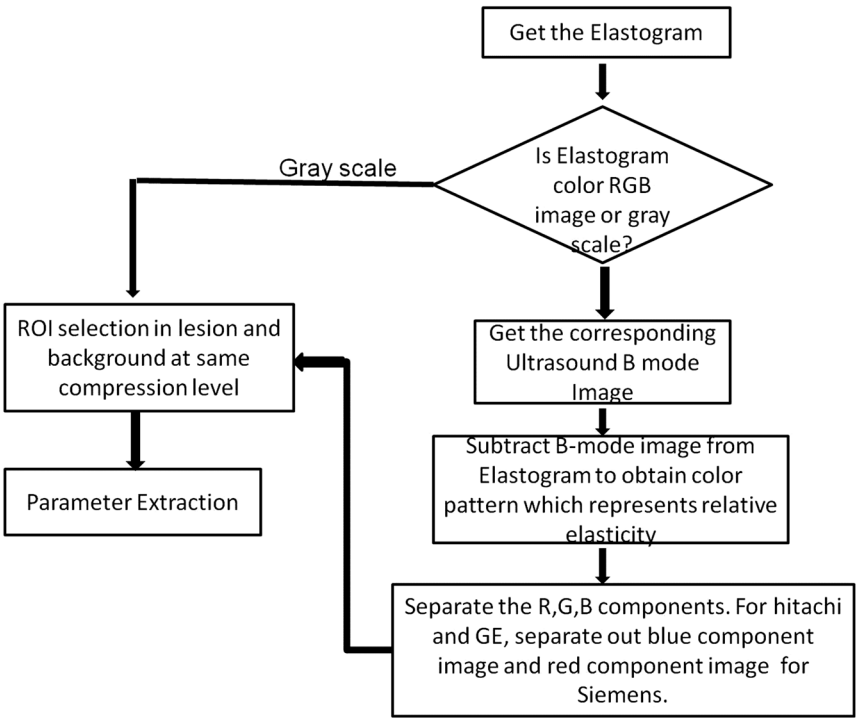

Fig. 6 Flowchart of the image processing algorithm.

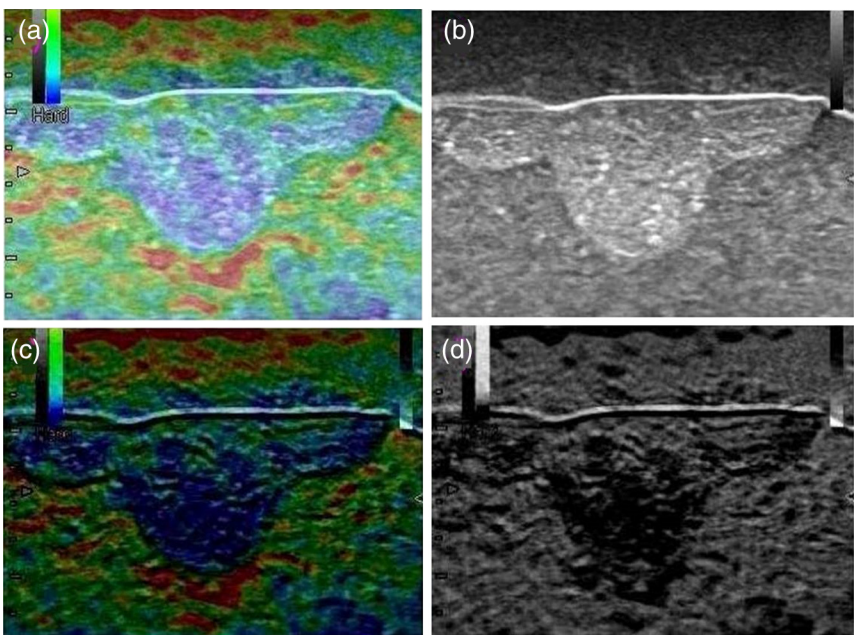

Fig. 7 Processing of color elastogram for Category II inclusions using the Hitachi machine to extract image-based parameters: (a) elastogram, (b) B-mode image, (c) color pattern, and (d) blue component image.

$$C_o = \frac{\mu_{bg}}{\mu_t}, \tag{7}$$

where μ_{bg} is the mean strain of the background and μ_t is the mean strain of the inclusion. CTE is the ratio of observed contrast to true modulus contrast and is expressed as

$$\mathrm{CTE} = \frac{C_o}{C_m}, \tag{8}$$

$$\text{in dB}, \mathrm{CTE(dB)} = |C_o(\mathrm{dB})| - |C_m(\mathrm{dB})|, \tag{9}$$

where C_m is the true modulus contrast (modulus of inclusion/modulus of background).

Observed strain contrast and CTE were computed for the ideal images obtained from 3-D FEM simulations and used to compare equivalent images obtained from the imaging experiments with the custom-made breast tissue-mimicking phantoms.

6 Results and Discussion

Based on the proposed phantom layout in Fig. 2, a total of 20 realizations of the phantom were made, each with four categories of inclusions, imaged by five expert radiologists and also used to train 30 novice radiologists. The average years of experience for expert radiologists was 15, and they regularly use elastography in their clinical practice. Novice radiologists include residents and other consultants who have familiarity with B-mode but are new to elastography. The phantoms were imaged using ultrasound B-mode and strain elastography in order to analyze the appearance of the prepared solid and cystic inclusions. All the four ultrasound elastography machines were used to acquire elastograms and B-modes. Sample images for all categories of inclusions by the four elastography scanners are shown in Fig. 8. There is a time gap in formulating all the layers since the phantom was prepared in three steps: we could notice a thin line of separation in the images. Those lines do not have any impact in elastogram or B-mode acquisition and further image contrast analysis, since these lines might be expected to introduce unnecessary artifacts. Elastograms are displayed along with the corresponding B-mode. The Category I (C1) lesion is hypoechoic in B-mode, which leads the sonographers to an incorrect conclusion, while the elastogram shows an isoelastic pattern, which improves the confidence of sonographers in their exclusion. The spiculations in malignant lesions are well represented in both B-mode and elastograms (C2) in all the four image sets. They have either blue or red components to represent less relative strain. Category III (C3) fibroadenoma lesions have a slight change in stiffness, which makes them difficult to distinguish from the background. Both bull's eye and BGR pattern are well appreciated for cystic lesions (C4). The acquired images were also verified by utilizing the semiquantification parameters, such as strain ratio (explained in Sec. 3), reported from the Hitachi machine. For all the fibroadenoma images, the strain ratio (the parameter reported by Hitachi machine as detailed in Sec. 2.2) was within 2, and for the

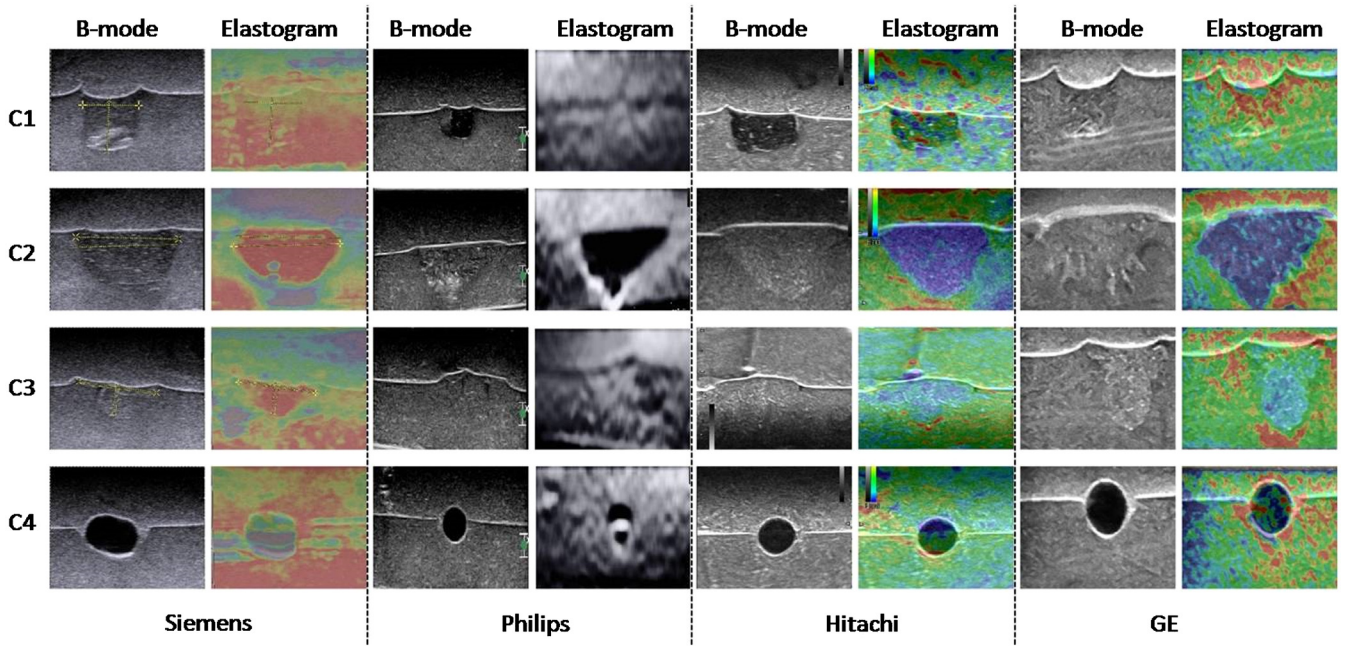

Fig. 8 Representative images of breast phantom from four ultrasound systems; C1, C2, C3, and C4 indicate four categories of inclusions.

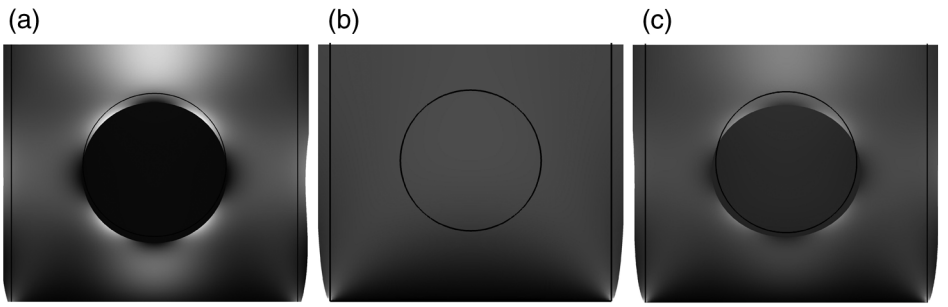

Fig. 9 Ideal strain images for (a) invasive ductal carcinoma, (b) suspicious glands, and (c) fibroadenoma. The black circular line represents the original position of the inclusion before compression.

definitely malignant category, the strain ratio was >8. The results are in good agreement with the *in-vivo* patient studies reported by Barr et al.[2]

The phantoms were also simulated using COMSOL and a linear material model. Solid inclusions were simulated in a homogeneous background, and the ideal strain images are shown in Fig. 9. Cystic lesions were not simulated in the present work. Simulation of a numerical model of cysts is a complex problem. Cystic fluid surrounded by a thin cystic membrane, which is also deformable, alters the displacement properties. This requires modeling of the fluid structure interaction with a deformable mesh. A coupled fluid analysis is required to analyze the interaction between solid motion and induced fluid flow within a cyst. The experimental and simulation results were corroborated for various machines. The results for observed strain contrast and CTE are the average of values calculated for 20 different realizations, and the error bars are the standard deviation from these estimates [Figs. 10(a) and 10(b)]. The results are presented in Table 3. High modulus contrast inclusions (>12 dB) or the Young's modulus of inclusions, which is >80 kPa, are exaggerated in terms of strain contrast. Other low contrast inclusions are represented within a tolerable range of strain contrast. Despite different machines following different protocols, the CTE presents similar trends. This supports the use of the prepared custom-made tissue mimicking phantom in clinical training.

Based on our study, we observed that strain elastography has several limitations. Adequate and standardized compression is an important feature that may influence the strain image quality. For all the machines, it is recommended that the probe should be in light contact with the surface during the elastogram acquisition because the stress and strain are no longer linearly proportional beyond a certain degree of deformation of the inclusion and boundary. Strain properties are highly altered depending on the precompression applied.[2,25] During acquisition, a sufficient amount of the surrounding normal background portion must be included at the same depth as inclusions to gain a right comparison. This is uncertain if the inclusion diameter is large. In addition, compression elastography approaches were associated with intra- and interobserver variability with regard to performing and interpreting elastosonographic data. Especially, it was influenced by operator dependence, because it requires some experience to obtain reproducible results. The use of the proposed phantom with inclusions similar to B-mode and elastographic appearance in current study might be a better standardization tool for inexperienced operators.

There are some limitations in the developed phantoms. In this work, we designed malignant cancers as regions with hyperechogenecity. However, in real time, most of the invasive ductal cancers are hypoechoic structures in B-mode images. In the agar

Table 3 Comparison of observed strain contrast across machines with finite-element model (FEM).

Category of the inclusion	Machine used	C_o(dB)	C_m(dB)
C1	Philips	-0.33 ± 0.09	0
	Siemens	1.2 ± 1.94	
	Hitachi	-0.58 ± 3.42	
	GE	0.89 ± 1.35	
	FEM	-0.8 ± 0	
C2	Philips	8.2 ± 1.66	6
	Siemens	4.3 ± 5.53	
	Hitachi	8.21 ± 0.586	
	GE	1.63 ± 2.03	
	FEM	4.2 ± 0	
C3	Philips	23.9 ± 1.73	25
	Siemens	36.6 ± 4.4	
	Hitachi	18.75 ± 3.66	
	GE	17.7 ± 8.15	
	FEM	18.3 ± 1.35	

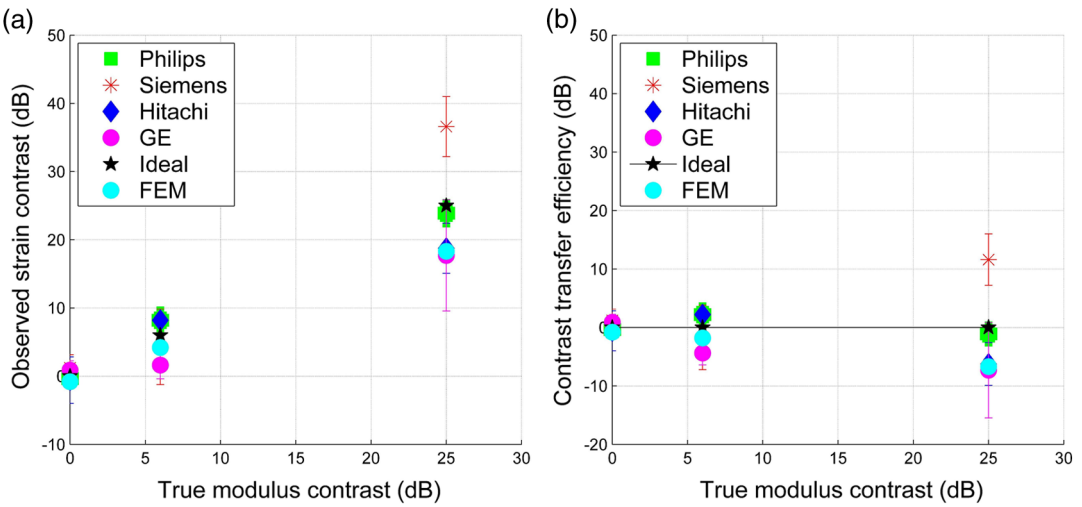

Fig. 10 (a) Observed strain contrast versus true modulus contrast and (b) contrast transfer efficiency versus true modulus contrast of phantom.

phantoms which are reported in this work, an increase in agar concentration will result in a stiffness increase. In addition to the stiffness increase, echogenecity is also increased with an increase in agar concentration due to the speckle-generating nature of agar particles. Hence, high modulus contrast inclusions have also become hyperechoic structures in the B-mode in this work. Even though the scattering properties of the background are increased by adding graphite, we could not achieve a complete hypoechoic malignant mimicking inclusion. In order to avoid this, we need a phantom material whose structural and scattering properties are independently controlled.

Cystic lesions are anechoic, and they generate bull's eye and BGR patterns in elastograms, with which they could be easily differentiated. But this was not valid when we dealt with large diameter cysts. Due to signal void at the middle, neither bull's eye nor BGR patterns were achieved.

In the future, the phantoms could be made to include other breast abnormalities like lipoma, breast necrosis, and all the BIRADS categories. In addition to simple cysts, complicated and complex cysts could be mimicked for training purposes. Due to the simplicity in the design procedure, this phantom could be made in clinical environments, and the preparation time is ~36 h. The phantoms could be made stable for more than 6 months by properly preserving them in a refrigerator by immersing them in deionized water.

7 Conclusion

A clinically relevant breast training phantom catering to the need of radiologists was made with four categories of inclusions. The sonographic and elastographic appearances of the inclusions were imaged using four different elastographic machines. An FEM model was created to mimic the experiment, and ideal strain images were created. Contrast and CTE were extracted from both model and experiment. The results show that high modulus contrast inclusions are well defined in elastography with improved contrast, whereas low contrast lesions are represented with reasonable contrast. The prepared phantom could be used as a training tool in hospitals. An observer study with a large number of radiologists, which includes comparison of clinical image quality metrics for the images obtained by untrained radiographers before and after training with the developed phantom is currently underway.

Acknowledgments

The first author would like to thank Dr. R. Kalpana Devi of Apollo Speciality Hospital for help in performing the image acquisition. Anonymous reviewers are greatly thanked for their very thorough and inspiring review, which substantially improved the quality of the manuscript.

References

1. S. Asthana, S. Chauhan, and S. Labani, "Breast and cervical cancer risk in India: an update," *Ind. J. Public Health* **58**, 5–10 (2014).
2. G. R. Barr, "Sonographic breast elastography a primer," *J. Ultrasound Med.* **31**, 773–783 (2012).
3. T. A. Krouskop et al., "Elastic moduli of breast and prostate tissues under compression," *Ultrsound Imaging* **20**, 260–274 (1998).
4. Y. C. Fung, *Biomechanics: Mechanical Properties of Living Tissues*, pp. 243–312, Springer Verlag, New York (1993).
5. J. Ophir, "Elastography: a quantitative method for imaging the elasticity of biological tissues," *Ultrasound Imaging* **13**, 111–134 (1991).
6. R. Muthupillai et al., "Magnetic resonance elastography by direct visualization of propagating acoustic strain waves," *Science* **269**, 1854–1857 (1995).
7. U. C. Devi, R. M. Vasu, and A. K. Sood, "Design, fabrication and characterization of a tissue equivalent phantom for optical elastography," *J. Biomed. Opt.* **10**, 044020 (2005).
8. K. Nightingale, R. Bentley, and G. E. Trahey, "Observations of tissue response to acoustic radiation force: opportunities for imaging," *Ultrasonic Imaging* **24**, 100–108 (2002).
9. R. Dickinson and C. Hill, "Measurement of soft tissue motion using correlation between a-scans," *Ultrasound Med. Biol.* **8**, 263–271 (1982).
10. J. Bercoff, M. Tanter, and M. Fink, "Supersonic shear imaging: a new technique for soft tissue elasticity mapping," *IEEE Trans. Ultrasonics Ferroelect. Freq. Control* **51**, 369–409 (2004).
11. G. Garra et al., "Elastography of breast lesions: initial clinical results," *Radiology* **202**, 79–86 (1997).
12. M. Kavitha et al., "Fuzzy-based classification of breast lesions using ultrasound echography and elastography," *Ultrasound Quart.* **28**, 159–167 (2012).
13. E. L. Madsen et al., "Tissue-mimicking agar/gelatin materials for use in heterogeneous elastography phantoms," *Phys. Med. Biol.* **50**(23), 5597 (2005).
14. L. A. Negron et al., "Development and characterization of vitreous mimicking material for radiation force imaging," *IEEE Trans. Ultrasonics Ferroelectr. Freq. Control* **49**, 1543–1551 (2002).
15. E. Brusseau et al., "Axial strain imaging of intravascular data: results on polyvinyl alcohol cryogel phantoms and carotid artery," *Ultrasound Med. Biol.* **27**(12), 1631–1642 (2001).
16. C. Martin et al., "A review of tissue substitutes for ultrasound imaging," *Ultrasound Med. Biol.* **36**, 861–873 (2010).
17. J. Oudry et al., "Copolymer-in oil phantom materials for elastography," *Ultrasound Med. Biol.* **35**, 1185–1197 (2009).
18. J. Fromageau et al., "Estimation of polyvinyl alcohol cryogel mechanical properties with four ultrasound elastography methods and comparison with gold standard testings," *IEEE Trans. Ultrasonics Ferroelectr. Freq. Control* **54**, 498–509 (2007).
19. "Breast elastography phantom model 059," http://www.cirsinc.com/products/all/83/breast-elastography-phantom/ (2005).
20. "Blue phantom specifications: elastography ultrasound breast phantom," http://www.bluephantom.com/product/Elastography-Ultrasound-Breast-Phantom.aspx?cid=380 (2011).
21. J. E. Browne et al., "Investigation of the effect of subcutaneous fat on image quality performance of 2D conventional imaging and tissue harmonic imaging," *Ultrasound Med. Biol.* **31**(7), 957–964 (2005).
22. S. Cournane, A. Fagan, and J. Browne, "Review of ultrasound elastography quality control and training test phantoms," *Ultrasound* **20**, 16–13 (2012).
23. E. L. Madsen et al., "Anthropomorphic breast phantoms for testing elastography systems," *Ultrasound Med. Biol.* **32**(6), 857–874 (2006).
24. K. Manickam, R. Machireddy, and S. Seshadri, "Study of ultrasound stiffness imaging methods using tissue mimicking phantoms," *Ultrasonics* **54**, 621–631 (2014).
25. K. Manickam, R. Machireddy, and S. Seshadri, "Characterization of biomechanical properties of agar based tissue mimicking phantoms for ultrasound stiffness imaging techniques," *J. Mech. Behav. Biomed. Mater.* **35**, 132–143 (2014).
26. J. Browne et al., "Assessment of the acoustic properties of common tissue mimicking test phantoms," *Ultrasound Med. Biol.* **29**, 1053–1060 (2003).
27. T. J. Hall et al., "Phantom materials for elastography," *IEEE Trans. Ultrasonics Ferroelect. Freq. Control* **44**, 13–1355 (1997).
28. A. Itoh et al., "Breast disease: clinical application of us elastography for diagnosis," *Radiology* **239**, 341–350 (2006).
29. A. T. Stavros et al., "Solid breast nodules: use of sonography to distinguish between benign and malignant lesions," *Radiology* **196**, 123–134 (1995).
30. G. Anderson, C. R. Ned, and M. L. Palmeri, "Effect of graphite concentration on shear-wave speed in gelatin-based tissue-mimicking phantoms," *Ultrasonics Imaging* **33**, 134–142 (2011).
31. T. Shiina et al., "Real time tissue elasticity imaging using the combined autocorrelation method," *J. Med. Ultrasound* **29**, 119–128 (2002).

32. M. Jones, *Mechanics of Composite Materials*, Taylor and Francis, New York (1998).
33. S. Saada, *Elasticity: Theory and Applications*, Pergamon Press, New York (1983).
34. E. Konofagou et al., "Reduction of stress nonuniformities by apodization of compressor displacement in elastography," *J. Ultrasound Med. Biol.* **22**, 1229–1236 (1996).
35. F. Kallel and J. Ophir, "Limits on the contrast of stress-concentrations in elastography," *Ultrasound Med. Biol.* **24**, 1215–1219 (1998).
36. F. Kallel, M. Bertrand, and J. Ophir, "Fundamental limitations on the contrast-transfer efficiency in elastography: an analytic study," *Ultrasound Med. Biol.* **22**, 463–470 (1996).
37. T. Varghese et al., "Tradeoffs in elastographic imaging," *Ultrasonics Imaging* **23**, 216–248 (2001).
38. S. Bharath and T. Varghese, "Contrast-transfer improvement for electrode displacement elastography," *Phys. Med. Biol.* **51**, 6403–6418 (2006).